

The Frequent Image Frames Enhanced Digital Orthorectified Mapping (FIFEDOM) Camera for Acquiring Multiangular Reflectance From the Land Surface

Baoxin Hu, *Member, IEEE*, K. Frank Zhang, Lawrence Gray, John R. Miller, and Harold Zwick

Abstract—The Frequent Image Frames Enhanced Digital Orthorectified Mapping (FIFEDOM) camera was designed to provide a cost-effective remote-sensing method for accurate acquisition of forest information, such as spatial distributions of individual tree species and tree structures for forest monitoring and management. Compared with existing regular digital cameras, the FIFEDOM camera has several unique features as follows: 1) it can collect data not only in the visible bands (550 and 670 nm) but also in the near-infrared band (800 nm); 2) it has a frame rate of up to 3 frames/s with a frame size of 3500×2300 ; and 3) it has a wide angular field view with 150° along track and 78.8° across track. Its high frame rate and wide angular field view allow it to obtain a sequence of images that oversample ground target areas. The multiangle database and bidirectional reflectance signatures of forest canopies can be generated from the oversampled image data, which can be used to identify forest species and estimate tree structures. In addition, the multiframe highly overlapped FIFEDOM data can also be used to generate a very dense, high-quality, and reliable digital surface model. Effective methods for radiometric and geometric calibration of the FIFEDOM camera were developed in this paper. A data-acquisition campaign was carried out in 2004 over the Algoma boreal forest, Ontario, Canada. The FIFEDOM data were validated using the data acquired by the Compact Airborne Spectrographic Imager instrument, which was flown together with the FIFEDOM camera.

Index Terms—BRDF, multi-angle, remote sensing, wide-angular-field-view camera.

I. INTRODUCTION

FOREST management and environmental monitoring require accurate forest information, such as spatial distributions of individual tree species and tree structures. Various remote-sensing techniques are available for deriving the architectural properties of vegetation canopies. For example, high spatial resolution multispectral systems have been explored as

cost-effective means of classifying forest species and measuring forest structural characteristics in a spatially and temporally continuous manner. However, these techniques ignore the information content implicitly associated with vertical forest canopy architectural properties. Synthetic aperture radar (SAR) has demonstrated great potential in assessing vegetation structural parameters like tree height, density, as well as crown characteristics [1], [2]. Although SAR techniques are independent of cloud cover and atmospheric conditions, both wind and precipitation affect the magnitude of the backscattered signal, simply by altering the structural and dielectric properties of the observed target [3]. In addition, factors such as the wavelength of the radar and the specific spectral response of plant elements affect the radar penetration depth, thus control the saturation limit and the feasibility of accurately retrieving information on canopy structure. Recently, light detection and ranging (LiDAR) remote sensing has attracted a lot of attention in forestry applications [4], [5]. While studies have shown that LiDAR observations of forest canopies can be used to derive many of the structural attributes, there is a lack of maturity in algorithms and models, mainly caused by the lack of airborne and spaceborne data and coincident ground measurements. Because LiDAR is relatively new as applied to canopy measurement (despite early studies using small-footprint LiDAR as far back as the work by Aldred and Bonner [6]), there is a tremendous need for experiments that integrate field work, remote sensing, and subsequent analyses for retrieving the full complement of structural measures critical for forestry applications. In addition, its applications are fairly limited due to its high operational and maintenance cost. Recently, the Multiangle Imaging SpectroRadiometer (MISR) data have been available for characterizing the anisotropic reflectance properties of surface objects [7], [8]. Structural properties of surface objects can be derived from their reflectance obtained from different angles. However, MISR's low spatial resolution (275×275 m) limits its use in forest managements in the local scale.

A cost-effective alternative for mapping 3-D structures of forest canopies is to use high frame rate digital cameras. Traditionally, the aerial camera exposes a sequence of 23×23 cm image frames, with typically 60% overlap from frame to frame along flight lines to ensure stereo coverage and with 30% sidelap to assume no missing coverage caused by aircraft

Manuscript received September 30, 2006; revised May 18, 2007. This work was supported in part by the Earth and Environmental Technologies (ETech), Natural Sciences and Engineering Research Council of Canada, and in part by the MacDonald, Dettwiler, and Associates, Ltd.

B. Hu, K. F. Zhang, L. Gray, and J. R. Miller are with the Department of Earth and Space Science and Engineering, York University, Toronto, ON M3J 1P3, Canada.

H. Zwick is with Macdonald, Dettwiler, and Associates, Richmond, BC V6V 2J3, Canada.

Color versions of one or more of the figures in this paper are available online at <http://ieeexplore.ieee.org>.

Digital Object Identifier 10.1109/TGRS.2007.904917

orientation instability and position uncertainty. Because of limitations of conventional cameras, as well as costs and inconvenience, more overlap is rarely acquired. The new high frame rate digital camera, however, could make it easy, cost-effective, and natural to collect multiband imagery with high overlaps. This means that the same area on the ground could be seen in many images. Moreover, because of the view geometry of frame cameras, each image looks at the same area on the ground from a slightly different angle [9]. If a wide-angle lens is mounted to the high frame rate digital camera, more overlapping can be achieved and more observations with different viewing angles can be acquired. The multiangle database and subsequent bidirectional reflectance signatures of forest canopies can be generated from the oversampled image data, which can be used to identify forest species and estimate tree structures. To realize the potentials of the high frame rate digital camera technology in forestry applications, the Frequent Image Frames Enhanced Digital Orthorectified Mapping (FIFEDOM) camera was designed to obtain the 3-D structural information of vegetation canopies by exploiting the redundancy properties of the digital aerial imagery.

The design principle of using the overlapping among along-track frames to generate angular signature of surface objects was first used in the Polarization and Directionality of the Earth's Reflectance (POLDER) instrument [10], [11]. POLDER's field view is 51° along track and 43° across track; its charge-coupled device (CCD) matrix is composed of 384×288 pixels; and the time laid between two successive shots is 10 s. Due to its small frame size and relatively slow frame rate, the airborne POLDER has been used to collect bidirectional reflectance data set over a large homogeneous area, such as the data sets acquired over the tower flux sites in the Boreal Ecosystem-Atmosphere Study areas [12]. FIFEDOM, employing a high frame rate digital camera, a large CCD array, and a wide field-of-view lens, will be able to acquire high spatial resolution angular data sets.

In this paper, the FIFEDOM design concept and procedures for radiometric and geometric calibrations are described. The FIFEDOM data acquired over the Algoma boreal forest, Ontario, Canada, in 2004 and the data validation results are also described in this paper.

II. CAMERA DESCRIPTION

Compared with the existing regular digital cameras, the FIFEDOM camera has several unique features as follows: 1) it can collect data not only in the visible bands (550 and 670 nm) but also in the near-infrared band (800 nm); 2) it has a frame rate of up to 3 frames/s with a frame size of 3500×2300 ; and 3) it has a wide angular field view with 150° along track and 78.8° across track. Its high frame rate and wide angular field view allow it to obtain a sequence of images that oversample ground target areas. As shown in Fig. 1, the area of interest on the ground can be viewed from about 75° in the forward direction to 75° in the backward direction along one flight line. Compared with a camera with a normal lens, whose view geometry is also shown in Fig. 1, more observations with different angles can be achieved for the same flight height and speed.

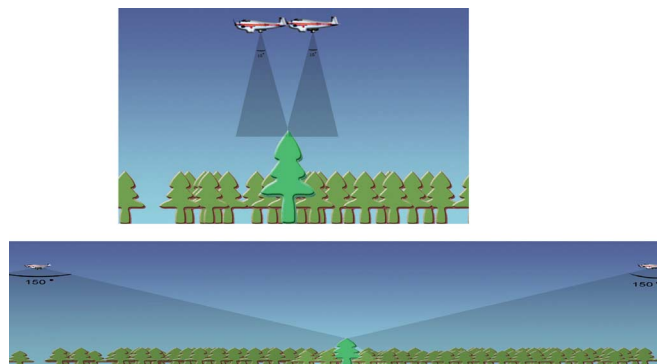


Fig. 1. Viewing geometries of a regular digital camera and the FIFEDOM camera.



Fig. 2. Overall view of FIFEDOM camera showing (from left to bottom) the shutter assembly with wide-angle lens, the field lens mount, the collimator lens, the filter wheel, and the CCD camera.

The design of the FIFEDOM camera is shown in Fig. 2. It consists of three lenses. The first one is a Zeiss Distagon 16-mm lens, which is a wide-angle lens, and is used as the telescope. The second and third lenses are both Nikkor 105 mm and served as collimators. A Uniblitz shutter was used to control the illumination. A CCD camera is attached at the end. The spectral filter, which is placed between the two collimators, alters every $1/3$ s to control the image wavelength. With a presettled time interval to move to the new location, three images in the wavelengths centered at 550, 670, and 800 nm are therefore taken over a target. The data are recorded in 3500×2300 Geo-TIFF format and have a radiometric resolution of 12 bits.

III. CALIBRATION

A. Radiometric Calibration

Like any other camera with a wide angular field of view, the FIFEDOM camera exhibits a large variation in the optical transmission of light across its image plane, which must be compensated before the data can be used for any scientific purpose. In addition, to extract quantitative information from the FIFEDOM data, the radiance at the camera for each pixel of the image frame also needs to be calculated. As a result, the radiometric calibration of the FIFEDOM camera was carried out in the following three steps: 1) measure its response uniformity; 2) measure the absolute camera response near the central

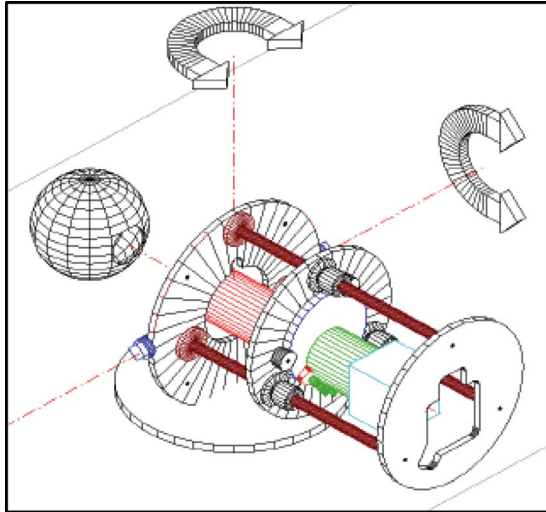


Fig. 3. FIFEDOM camera in rotation jig facing the uniform light source for the purpose of radiometric calibration.

region of the camera's field of view using a well characterized and calibrated standard source; and 3) use the uniformity map to relate the absolute measurement near the center to the entire field of view.

Due to the wide angular field of view of the FIFEDOM camera, measuring the uniformity of its radiometric response is not a trivial task. There are no suitable sources available to fill the entire field of view. As a result, an integrating sphere was used to undertake a piecewise mapping of the response across the image plane of the camera. The integrating sphere, which is called precision diffuse source (PDS), is a well-characterized uniform source that exhibits very little variation ($< 0.1\%$) when viewing the exit aperture at restricted angles ($< \pm 10^\circ$). It has a 3-in diameter exit aperture. The square subtended by the aperture has a dimension of 2.12 in. It seems reasonable to rotate the camera to mosaic the subtended square of the sphere's exit aperture across the image plane. The areas outside provide the overlap necessary to correct for temporal variation of the source and fluctuations in the timing of shutter exposure. In order to complete these measurements, the FIFEDOM camera was placed in a designed rotation jig, as shown in Fig. 3. The jig allowed the camera to rotate in pitch and yaw directions ($\pm 80^\circ$ and $\pm 55^\circ$, respectively). The segment images of the PDS sphere were merged to generate the full radiometric correction template. The uniformity response maps for the near-infrared, red, and green channels are shown in Fig. 4.

B. Geometric Calibration

Since the FIFEDOM camera consists of a wide angular "fish-eye" lens, issues related to the geometry of a fish-eye lens have to be addressed during the geometric calibration procedure. Fish-eye lenses are designed to cover the whole hemispherical area in front of the camera, and it is impossible to image its whole field of view on a finite image plane by a perspective projection. Therefore, a fish-eye lens is usually designed to obey other projection models. Among them are stereographic projection, equidistance projection, equisolid angle projection;

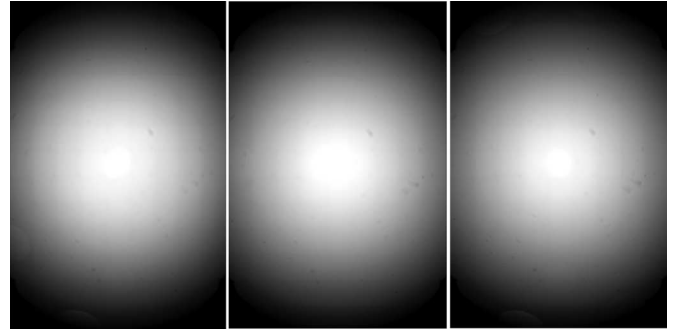


Fig. 4. Uniformity response maps of the FIFEDOM camera for the (left) near-infrared, (middle) red, and (right) green channels.

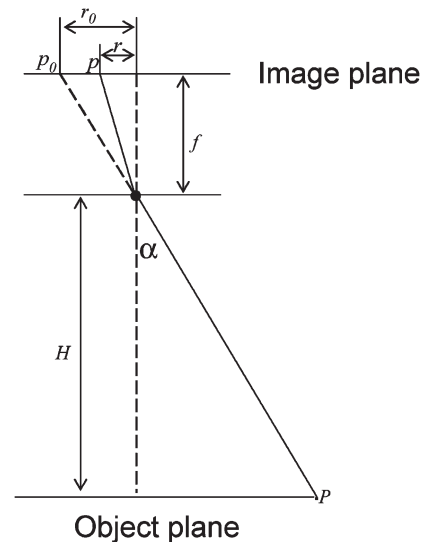


Fig. 5. Geometries of the perspective projection and equidistance projection. P is the object point. p_0 and p are the image points of point P under the perspective and equidistance projections, respectively. r_0 and r are their corresponding distances from the principal point. f is the focal length. H is the distance between the camera and the object plane. α is the angle between the optical axis and the incoming ray from point P .

and orthogonal projection [13]. However, a real lens does not exactly follow its designed projection model. As a result, the geometric calibration needs to determine the camera's projection model. Fig. 5 shows the perspective projection and the equidistance projection, a common model adopted by fish-eye lenses. The differences in the image positions under these two different projections are clearly observed. This distortion is often referred to as "fish-eye distortion," which needs to be modeled.

For the FIFEDOM camera, both the equidistance projection and the equisolid angle projection were tested, and a modified equidistance projection, which is described in (1), was used

$$r = k\alpha. \quad (1)$$

In (1), r is the distance between the image point and the principal point; α is the angle between the optical axis and the incoming ray, as shown in Fig. 5. The coefficient k was

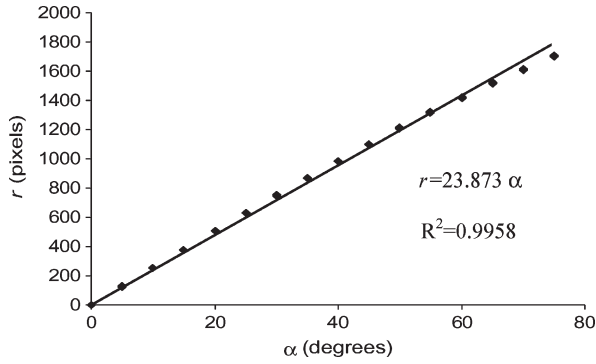


Fig. 6. Equidistance model [(1)] used to describe the projection of the FIFEDOM camera. Both α and r are shown in Fig. 5. Please note that α is in degrees and r is in pixels.

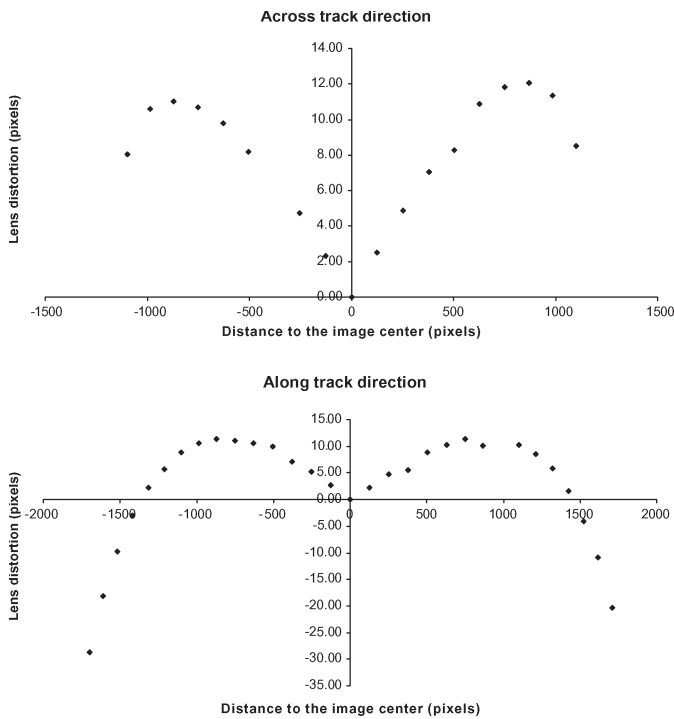


Fig. 7. Measured geometric distortions in the across-track and along-track directions. For the panel with the distortion in the across-track direction, the x -coordinate of each point is the horizontal distance in pixels between the position of this point in the image and the image center. If this point is at the right half of the image, its distance is positive. For the panel with the distortion in the along-track direction, the x -coordinate of each point is the vertical distance in pixels between the position of this point in the image and the image center. If this point is at the top half of the image, its distance is positive.

introduced to replace f (the focal length) in the original equidistance projection model.

Two polynomial equations, shown in (2) and (3), were used to model the “fish-eye” distortion and the normal-lens distortions, such as the radial and decentering distortions

$$\Delta x = x - x_0 = a_0 + a_1x + a_2x^2 + a_3x^3 + a_4x^4 \quad (2)$$

$$\Delta y = y - y_0 = b_0 + b_1y + b_2y^2 + b_3y^3 + b_4y^4. \quad (3)$$

In (2) and (3), $a_0, a_1, a_2, a_3, a_4, b_0, b_1, b_2, b_3,$ and b_4 are coefficients. The x -axis is along the across-track direction, and

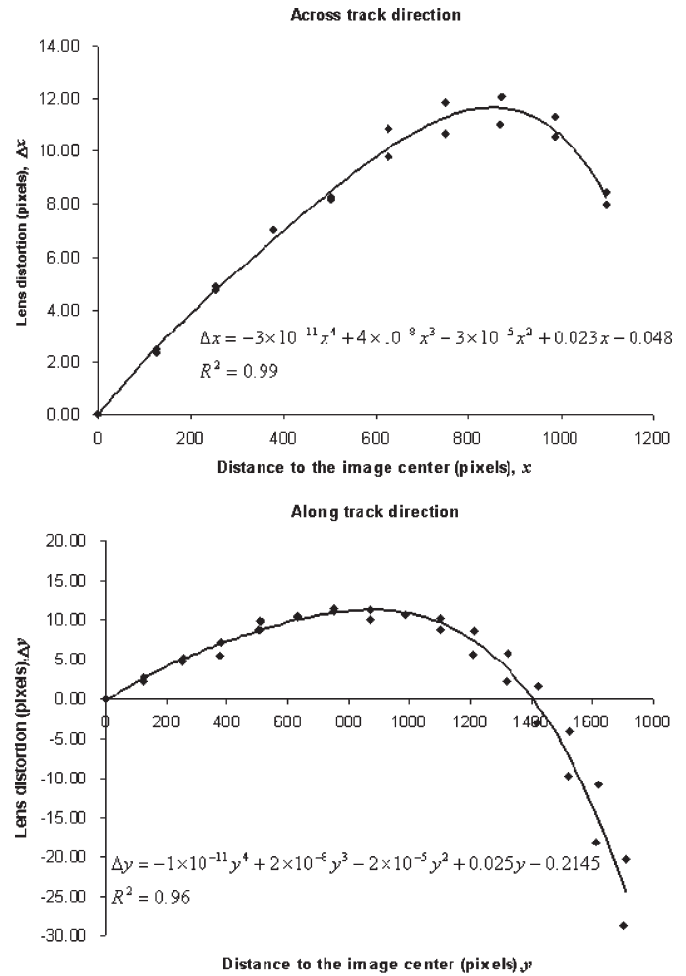


Fig. 8. Modeled distortions in the across-track and along-track directions. The dots are measured distortions determined by the image positions of the PDS sphere for different camera orientations and the corresponding image positions under perfect perspective projection. The solid line is the modeled distortions.

y -axis is along the along-track direction. (x, y) and (x_0, y_0) are the coordinates of the points p and p_0 in Fig. 5, respectively. Δx and Δy are the distortions in the along-track and across-track directions, respectively.

In order to determine the coefficients in (1)–(3), the same PDS sphere and mounting jig used for radiometric calibration were employed. Starting from the position and orientation where the PDS was imaged at the center of the FIFEDOM image plane, the camera was rotated in the horizontal (from center to right and from center to left) and vertical directions (going up from the center and then going down from the center) by a step of 5° . At each camera orientation, the image of the integrated sphere was captured. The position and orientation of the camera were recorded. The coordinates of the image point of the PDS in the image plane, denoted as (x, y) , were recorded as well. These data were used to determine coefficient k in (1), and the result is shown in Fig. 6. It is clear that the equidistance model can describe the lens projection very well (with an R^2 of 0.9958). k was determined as 23.873.

For each camera orientation, the coordinate of the image point of the PDS sphere projected by a pinhole camera (under

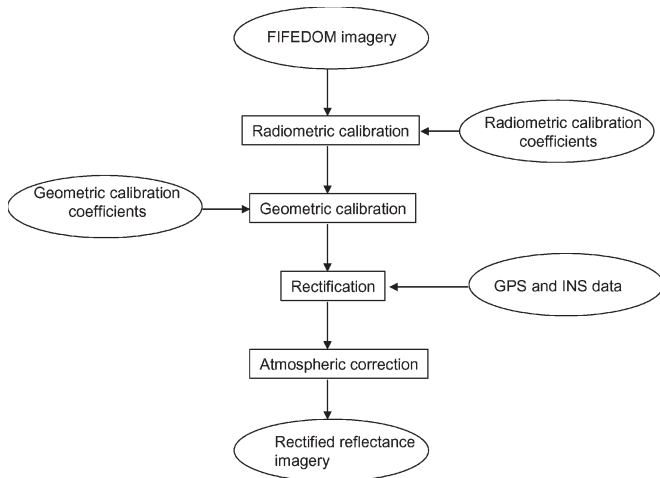


Fig. 9. Procedures for processing of the FIFEDOM data.

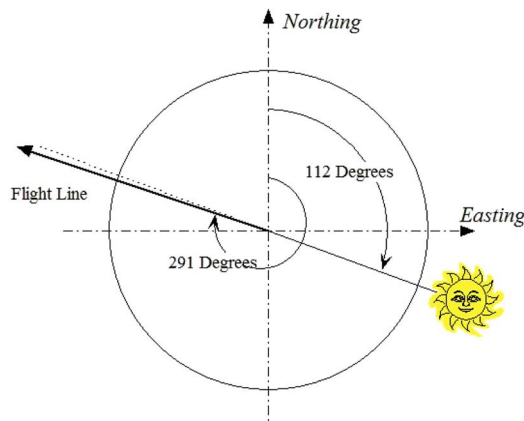


Fig. 10. Flight line over the study area dominated by black spruce canopies. The solar zenith angle is 48° . The flight was close to the solar principal plane.

the perspective projection and without lens distortions) was calculated using the collinearity equations [11] and is denoted as (x_0, y_0) . With a set of coordinates of (x, y) and (x_0, y_0) , the camera distortions, including “fish-eye” and other normal-lens distortions, were calculated and are shown in Fig. 7. In this figure, the positive direction is from the center to the right in the across-track direction and from the center to the top in the along-track direction. From Fig. 7, one can notice that the measured distortions are slightly asymmetric in both across-track and along-track directions, which is mainly caused by the imprecise camera positioning. Considering that the distortions tend to be symmetric, we used the two sets of data together without taking into account their directions. With these points shown in Fig. 7, the coefficients in (2) and (3) were determined. The modeled results are shown in Fig. 8, where the dots are measured distortions and the solid line is the modeled result. As shown in Fig. 8, the models given in (2) and (3) are effective to describe the FIFEDOM distortions. After correcting the distortions, the FIFEDOM images can be used up to 45° in the across-track direction with geometric errors within one pixel and up to 65° in the along-track direction with geometric errors within two pixels.

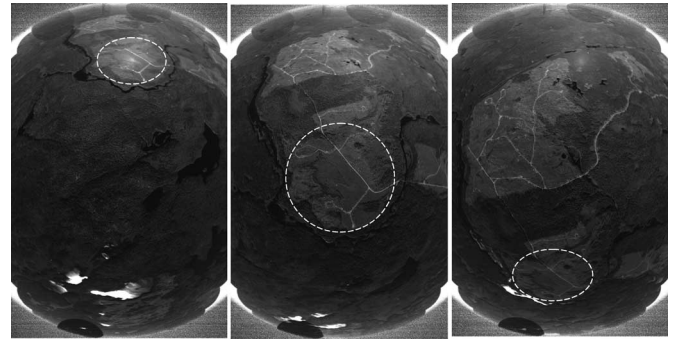


Fig. 11. Three images (after radiometric calibration) along the flight line (shown in Fig. 10) in the green band (550 nm). These images were taken while the aircraft flew away from the sun along the solar principal plane. The circled area is the study area dominated by the black spruce stands, which shows the same ground area viewed by the camera at different angles when the aircraft flew by. Please note that there are totally 12 images covering this study area.

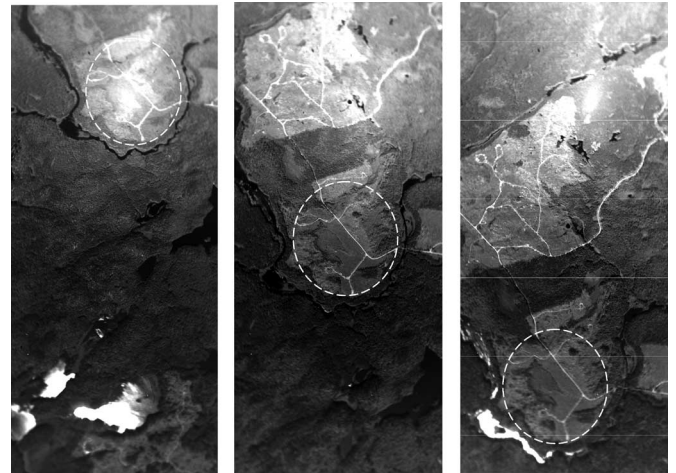


Fig. 12. FIFEDOM images after correcting camera geometric distortions, including the “fish-eye” and normal-lens distortions.

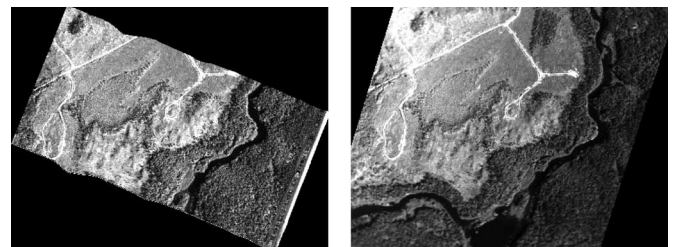


Fig. 13. Images in the green band (550 nm) acquired (left) by CASI and (right) FIFEDOM.

IV. DATA PROCESSING AND VALIDATION

During data acquisition, the FIFEDOM camera is fixed in a designed jig facing downward to the ground under the aircraft and can be integrated with an onboard inertial navigation system (INS) and GPS. The INS and GPS provide accurate positions and orientations of the exposure stations. With the exterior orientation parameters, the FIFEDOM image can be rectified using bundle adjustment [14]. These rectified images over the same ground areas will provide a multiangular data set. Fig. 9 shows the FIFEDOM data-processing procedures. A FIFEDOM toolbox was developed to perform these processing

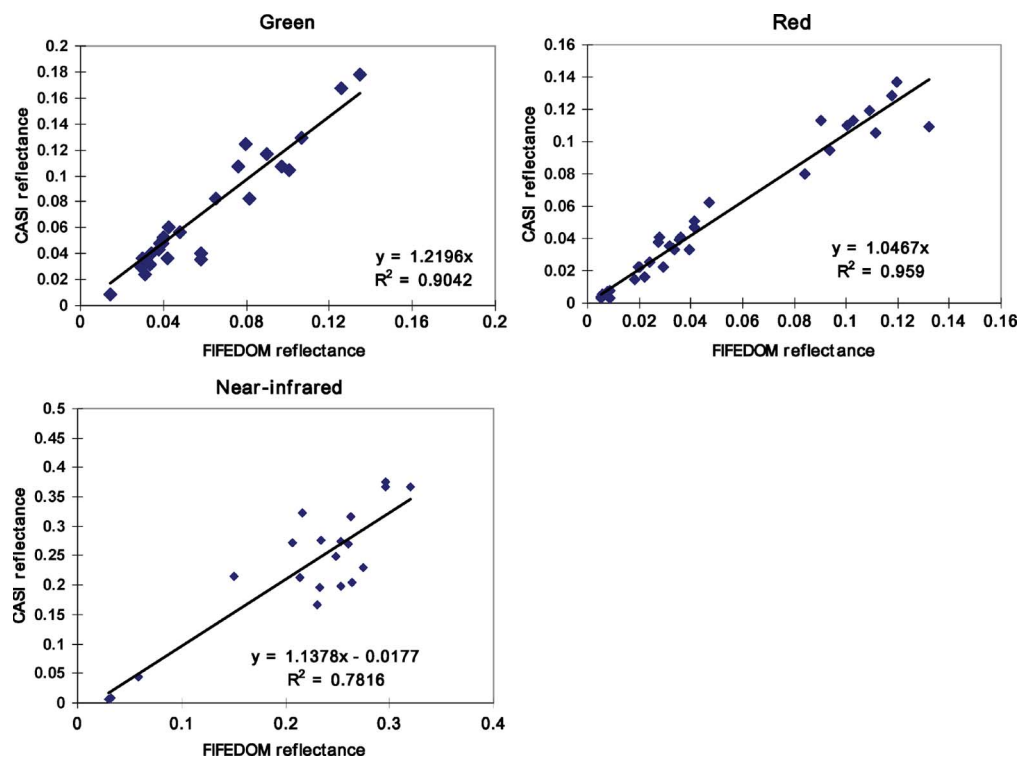


Fig. 14. Relationship between the CASI reflectance and the FIFEDOM reflectance in the green, red, and near-infrared bands.

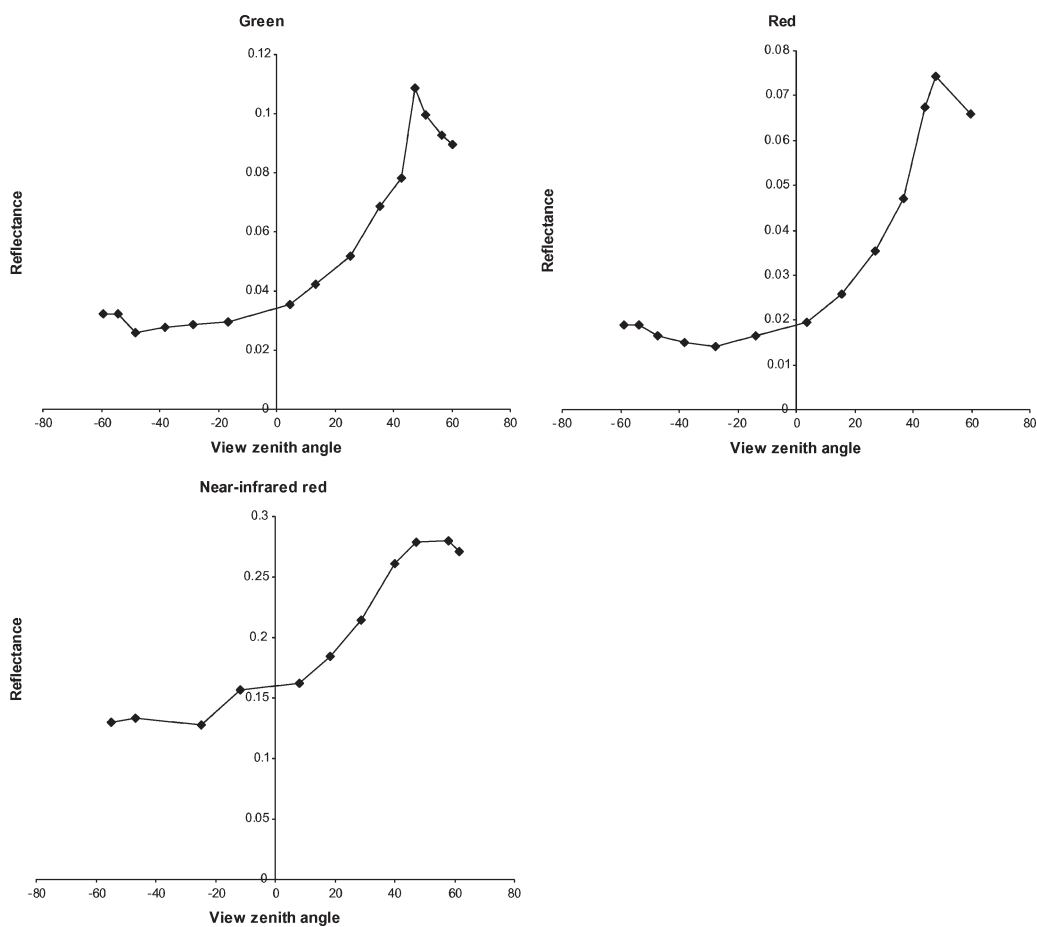


Fig. 15. Reflectance of a black spruce canopy at different view angles in the green, red, and near-infrared bands. The solar zenith angle is 48° , and the flight was roughly on the solar principal plane. The view angles are positive when the sun is behind the aircraft.

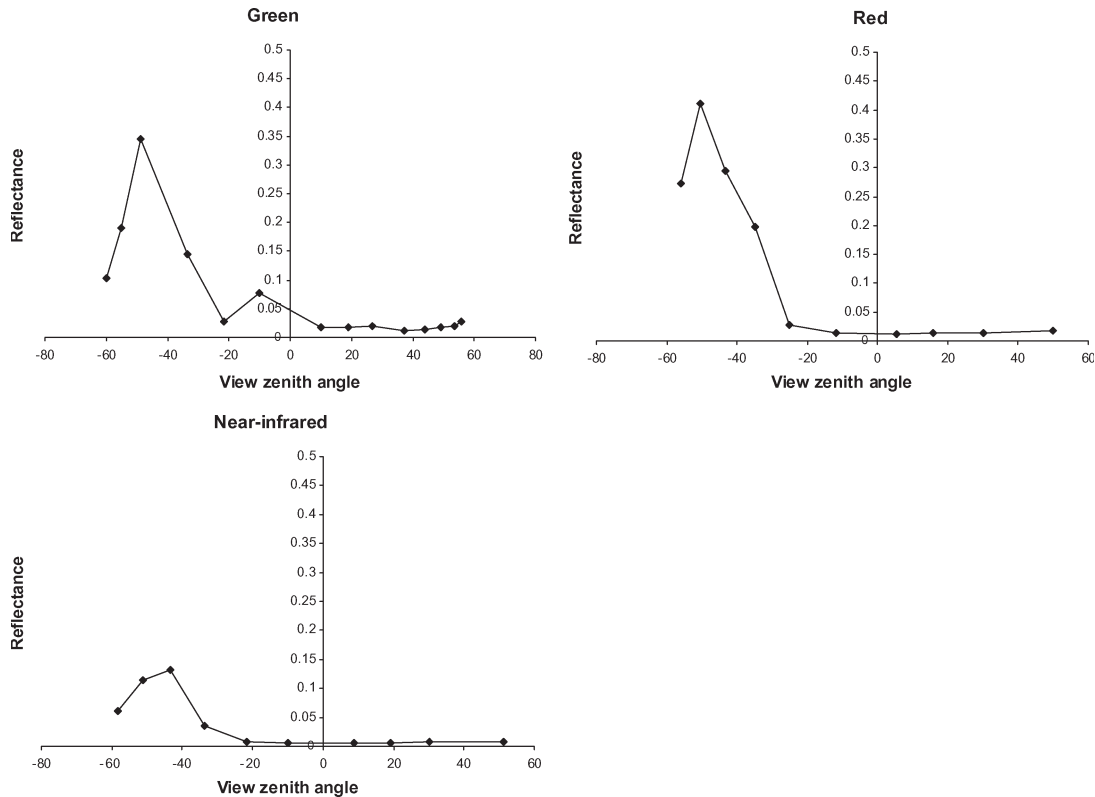


Fig. 16. Water reflectance at different view angles in the green, red, and near-infrared bands. The solar zenith angle is 48° , and the flight was roughly on the solar principal plane. The view angles are positive when the sun is behind the aircraft.

procedures. The inputs are the FIFEDOM raw data, an ASCII file containing GPS/INS data, and the radiometric and geometric calibration coefficients. The outputs are all of the rectified images over the area of interest and the view geometries of each pixel in these images. These outputs can be used to generate multiangle data sets for the study area. Multiangular observations of the reflectance anisotropy have been proven to be diagnostic for structural surface properties, which are helpful to complement the spectral measurements for a complete and robust characterization of a vegetation canopy.

A test flight of the FIFEDOM camera was carried out over the Algoma boreal forest, Ontario, Canada, in August 2004. The camera was mounted on a Piper Navajo Chieftain PA-350. The flight altitude was 4000 ft, and the speed was 130 kn. The data were taken while the aircraft flew away from the sun roughly along the solar principal plane with the solar zenith angle around 48° . As an example, the flight line over a study site dominated by black spruce stands was shown in Fig. 10. Three FIFEDOM images along this flight line are shown in Fig. 11. The circled areas cover the black spruce site. There are totally 12 images along this flight covering this study area. From Fig. 11, it is evident that there is a large degree of overlapping between images, and the same ground area (such as the circled area) can be viewed by the camera from different directions. For the left, middle, and right images in Fig. 11, the circled area was viewed with the sun behind the aircraft, at nadir, and with the aircraft facing the sun, respectively. As a result, the circled area appears brighter in the left image than in the other images, since less shadow was observed. The

specular reflection on the water bodies can be clearly observed from the right image. The geometric distortions are also evident in the images, as expected. Fig. 12 shows the images after correcting the geometric distortions, including the “fish-eye” and the normal-lens distortions. One can see from Fig. 12 that all of the geometric shapes in the three images appear the same, no matter where these shapes are located in the images. Please note that the geometric distortions caused by the perspective projection still exist in the images at this stage. The georectified FIFEDOM image was shown in Fig. 13 and compared with the image acquired by the Compact Airborne Spectrographic Imager (CASI) instrument over the same area. The spatial patterns and shapes exhibited in the FIFEDOM images are the same as those in the CASI image.

With the CASI images, radiometric validation of the FIFEDOM data was carried out as well. A small random set of pixels was used as test samples. The relationship between the CASI reflectance and FIFEDOM reflectance was shown in Fig. 14 for the green, red, and near-infrared bands. FIFEDOM reflectance is strongly correlated with CASI reflectance for the green and red bands, with R^2 values larger than 0.9. The R^2 is relatively smaller (0.78) for the near-infrared band. During the data acquisition, a problem occurred to the near-infrared filter, which leads to a certain degree of blurring in the near-infrared images. This is the main reason for the low R^2 value. This problem will be fixed for future data acquisition.

To further validate the FIFEDOM data, the angular signatures of some cover types were examined. Small relative homogeneous areas for black spruce stands and water bodies

were selected, and the reflectance values from these areas observed from different view angles were plotted. The results are shown in Figs. 15 and 16 for the black spruce stand and water, respectively. The strong backscattering (hotspot) and forward scattering (specular reflection) are exhibited in the angular signatures from the black spruce stand and water, respectively, as expected.

V. CONCLUSION

The FIFEDOM camera and its data analysis toolbox are the innovative development of integrating the aerial photogrammetry and remote sensing to specifically address issues in forestry management, such as accurately mapping forest species and forest structural parameters by providing multiangular data over the target area. The high spatial resolution FIFEDOM data can also help us to better interpret multiangle satellite data, such as those obtained by MISR.

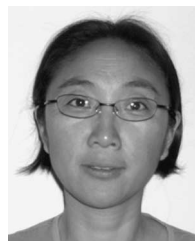
A test flight was conducted in 2004, and the analysis results proved the design concept and the effectiveness of the calibration procedures. Detailed validation and analysis are underway by comparing the FIFEDOM data and CASI data over the same area. In a future study, the radiometric and geometric calibration procedures will be further improved based on the validation results, and the FIFEDOM data will be analyzed to generate images of tree structures.

ACKNOWLEDGMENT

The authors would like to thank the financial and in-kind support provided for this paper through the Earth and Environmental technologies, Natural Sciences and Engineering Research Council of Canada, and MacDonald, Dettwiler, and Associates, Ltd.

REFERENCES

- [1] R. N. Treuhaft and P. R. Siquera, "Vertical structure of vegetated land surfaces from interferometric and polarimetric radar," *Radio Sci.*, vol. 35, no. 1, pp. 141–178, 2000.
- [2] T. Le Toan, A. Beaudoin, J. Riou, and D. Guyon, "Relating forest biomass to SAR data," *IEEE Trans. Geosci. Remote Sens.*, vol. 30, no. 2, pp. 403–411, Mar. 1992.
- [3] S. E. Hobbs, W. Ang, and C. Seynat, "Wind and rain effects on SAR backscatter from crops," in *Proc. 2nd Int. Workshop Retrieval Bio-Geophys. Parameters From SAR Data Land Appl.*, Oct. 21–23, 1998, pp. 185–189.
- [4] R. O. Dubayah and J. B. Drake, "LiDAR remote sensing for forestry," *J. For.*, vol. 98, no. 6, pp. 44–46, Jun. 2000.
- [5] M. Nilsson, "Estimation of tree heights and stand volume using an airborne LiDAR system," *Remote Sens. Environ.*, vol. 56, no. 1, pp. 1–7, Apr. 1996.
- [6] A. Aldred and M. Bonner, "Application of airborne lasers to forest surveys," Can. For. Service, Petawawa Nat. For. Centre, Chalk River, ON, Canada, Inf. Rep. PI-X-51, 1985, 62p.
- [7] D. J. Diner, J. C. Beckert, G. W. Bothwell, and J. I. Rodriguez, "Performance of the MISR instrument during its first 20 months in Earth orbit," *IEEE Trans. Geosci. Remote Sens.*, vol. 40, no. 7, pp. 1449–1466, Jul. 2002.
- [8] N. Gobron, B. Pinty, M. M. Verstraete, J.-L. Widlowski, and D. J. Diner, "Uniqueness of multiangular measurements—Part 2: Joint retrieval of vegetation structure and photosynthetic activity from MISR," *IEEE Trans. Geosci. Remote Sens.*, vol. 40, no. 7, pp. 1574–1592, Jul. 2002.
- [9] H. Wehn, N. Goldstein, B. Ameri, A. Moshkovitz, and H. Zwick, "Frequent-Image-Frames Enhanced Digital Ortho-Rectified Mapping (FIFEDOM) airborne mapping system," in *Proc. IGARSS*, Toronto, ON, Canada, 2002, pp. 1296–1298.
- [10] P.-Y. Deschamps, F. M. Breon, M. Leroy, A. Podaire, A. Bricaud, J. C. Buriez, and G. Seze, "The POLDER mission: Instrument characteristics and scientific objectives," *IEEE Trans. Geosci. Remote Sens.*, vol. 32, no. 3, pp. 598–615, May 1994.
- [11] M. Leroy and F. M. Breon, "Surface reflectance angular signatures from airborne POLDER data," *Remote Sens. Environ.*, vol. 57, no. 2, pp. 97–107, Aug. 1996.
- [12] P. M. Bicheron, M. Leroy, O. Hautecoeur, and F. M. Breon, "Enhanced discrimination of boreal forest covers with directional reflectances from the airborne polarization and directionality of Earth reflectances (POLDER) instrument," *J. Geophys. Res.* 102, no. 24, pp. 29 517–29 528, 1997.
- [13] J. Kannala and S. S. Brandt, "A generic camera model and calibration method for conventional, wide-angle, and fish-eye lenses," *IEEE Trans. Pattern Anal. Mach. Intell.*, vol. 28, no. 8, pp. 1335–1340, Aug. 2006.
- [14] P. R. Wolf, *Adjustment Computations: Statistics and Least Squares in Surveying and GIS*, 3rd ed. New York: Wiley-Interscience, 1996.



Baoxin Hu (M'06) received the B.Eng. and M.Eng. degrees in electrical engineering from Tianjin University, Tianjin, China, in 1987 and 1990, respectively, and the Ph.D. degree from Boston University, Boston, MA, in 1998.

From 1998 to 2003, she was a Visiting Scientist in the Canadian Space Agency, Canada. Since 2003, she has been with the Department of Earth and Space Science and Engineering, York University, Toronto, ON, Canada. Her current research interests

are canopy reflectance modeling, retrieval of biophysical parameters of vegetation canopies from remote-sensing data, analysis of hyperspectral remote-sensing data, and light detection and ranging remote sensing and its applications.



K. Frank Zhang received the B.Sc. degree in geomatics engineering and the M.Sc. degree in Earth and space science from York University, Toronto, ON, Canada, in 2005 and 2007, respectively, where he is currently working toward the Ph.D. degree in the Department of Earth and Space Science and Engineering, working on light detection and ranging modeling and canopy structure parameters retrievals.



Lawrence Gray received the B.Sc. degree in chemistry from the University of Toronto, Toronto, ON, Canada, in 1971.

He continued working as a gas chromatography–mass spectrometry and liquid chromatography–mass spectrometry analyst with the University of Toronto, developing trace atmospheric analytical services. Subsequently, he worked with Moniteq Ltd., where he was involved in the development and field trials of remote-sensing instrumentation. At Crestech [Institute for Space and Terrestrial Science (ISTS)], he

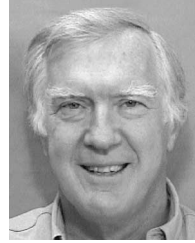
continued the development of optical analytical instrumentation and radiometric calibration techniques of imaging spectrometers. His expertise at deploying and operating airborne imaging systems is currently being employed with York University, Toronto, ON, Canada, developing the current York Frequent Image Frames Enhanced Digital Orthorectified Mapping system and light detection and ranging systems for trace atmospheric gas monitoring.



John R. Miller received the B.E. degree in physics and the M.Sc. and Ph.D. degrees in space physics from the University of Saskatchewan, Saskatoon, SK, Canada, in 1963, 1966, and 1969, respectively, studying the aurora borealis using rocket-borne radiometers.

He spent two years on a Postdoctoral Fellowship with the Herzberg Institute, National Research Council, Ottawa. He was with the faculty in the Department of Earth and Space Science and Engineering, York University, Toronto, ON, Canada, in

1972, where he is currently Professor of physics and Earth and space science. His remote-sensing interests include atmospheric correction and extraction of biophysical surface parameters through radiative transfer models from water color reflectance and from canopy reflectance for forestry and agriculture applications. Over the past two decades, his primary focus has been on the application of reflectance spectroscopic techniques in remote sensing using imaging spectrometer sensors.



Harold Zwick received the advanced degrees in physics and mathematics from the University of Saskatchewan, Saskatoon, SK, Canada. His academic research involved the development of Fabry-Pérot and Michelson interferometers to study the Earth's upper atmosphere and Aurora Borealis.

Between his Master's and Doctorate degrees, he worked for a time as a Radiation Physicist with the Radiology Department, Royal Victoria Hospital, Montreal, where he helped McGill University to develop Canada's first linear electron accelerator for

cancer therapy. After his academic studies, he was with Barringer Research Ltd., Toronto, where he developed trace gas remote-sensing instruments for geophysical and environmental applications. He later did research at the Canada Centre for Remote Sensing, Ottawa, where he developed and evaluated Earth Observation remote-sensing instrumentation, particularly pushbroom optical imagers for water quality and water depth applications. He next took a senior management position with Moniteq Ltd., Toronto, where he combined senior management activities with the development of Canada's first airborne imaging spectrometer instrument for Earth Observation. Since 1986, he has been the Principal Engineer with MacDonald, Dettwiler, and Associates (MDA), Richmond, BC, Canada, where he has held various technical and management positions. Since 2000, he has been managing the Corporate Research and Development Division, MDA, with responsibility of leading the new products and services development.